Numerical and experimental study on heat transfer and flow features of representative molten salts for energy applications in turbulent tube flow

Yu Qiu, Ming-Jia Li, Meng-Jie Li, Hong-Hu Zhang, Bo Ning

Numerical and experimental study on heat transfer and flow features of representative molten salts for energy applications in turbulent tube flow

Yu Qiu, Ming-Jia Li *, Meng-Jie Li, Hong-Hu Zhang, Bo Ning

Key Laboratory of Thermo-Fluid Science and Engineering of Ministry of Education, School of Energy and Power Engineering, Xi'an Jiaotong University, Xi'an, Shaanxi, 710049, China

* Corresponding author

Abstract: This article investigated the heat transfer performance and flow friction of the molten salts in turbulent tube flow, where four salts including Hitec, Solar Salt, NaF-$NaBF_4$, and FLiNaK were studied. A computational model was developed to analyze the flow and heat transfer features of the salts in the tube, and experiments were conducted to test the heat transfer performance of a representative salt Hitec in the tubes of a salt-oil heat exchanger. Comparison of simulation results with the experimental data shows that the average errors are smaller than ±4%, which validates the simulation model. Based on the model, firstly the influences of heat flux uniformity at the tube outer wall were examined. The results show that the non-uniform wall flux can lead to local high- temperature region but influences little on the flow friction coefficient and the heat transfer performance. Then, the model was utilized to investigate the friction and heat transfer features of the salts under broad ranges of the temperature and the velocity. Comparisons of the simulated heat transfer results with Hansen's, Sider-Tate's and Gnielinski's correlations show that the largest errors can reach +25%, +13% and -15%, respectively. Furthermore, the errors between the simulated friction coefficients and the Filonenko's correlation are smaller than ±2%, which indicates that this correlation is suitable for predicting the friction of the salts. Finally, to predict the heat transfer performance more accurately for these representative salts, a new correlation was developed. It was found that the errors between all simulation results and the proposed correlation are smaller than ±5%, while the corresponding values for 80% experiment data of three salts are also lower than ±5%. The current study can offer beneficial results and correlation for the applications of liquid salts in energy systems.

Keywords: Liquid salts; Heat transfer performance; Friction factor; Concentrating solar power; Nuclear energy

1. Introduction

In recent years, solar energy and nuclear energy have been considered as two promising

alternatives to reduce the severe global warming[1] and environment pollutions[2] induced by the utilization of fossil energy[3-5]. For the utilization of solar energy, a solar power generation technology called Concentrating Solar Power(CSP) that generates electric power by concentrating sun rays has developed rapidly during the past two decades[6, 7]. In this technology, molten nitrate salts are the most commonly used heat transfer fluids and heat storage mediums [8-10]. For nuclear energy, molten fluoride salts are considered as promising heat transfer fluids in the state-of-the-art fourth-generation nuclear plant[11, 12]. This is because the molten salts have numerous advantages such as low vapour tension, good thermostability, and low price[13, 14].

Liquid salts are usually employed to flow in round tubes of the heat exchangers and solar receivers in nuclear and CSP technologies. For improving the performance and ensuring the safe operation of these devices, it is necessary to understand the flow and heat transfer features of the liquid salts in the commonly used round pipe. As a result, numerous previous studies have investigated this topic using experiments.

A review of the previous work found that several experiments had investigated the heat transfer performance of some liquid salts in round pipes heated by uniform wall flux from the 1940s to 1970s. Typical liquid fluorides including ThF_4-BeF_2-UF_4-LiF [15, 16], FLiNaK [17-19] and NaF-$NaBF_4$ [15], and liquid nitrate Hitec [20, 21] had been experimentally studied. The data were compared with several classical correlations, but controversial conclusions were procured in different studies. Some studies found that some classical correlations are applicable for liquid salts[15, 16], while others procured opposite conclusion[17, 18]. During the following thirty years, there was almost no progress on this topic, and no experiment result had been openly reported.

However, in recent years, heat transfer of liquid salts has become a highlighted research area again. This is mainly due to the fast developments of CSP and nuclear technologies, where reliable heat transfer data and correlations with high accuracies are highly desired for the designs of heat transfer devices. From 2009 to now, the heat transfer performance of two liquid salts has been investigated by testing some shell-and-tube heat exchangers(STHX) when the salt flows in the tubes, where Hitec[13, 22-26] and $LiNO_3$[22, 27, 28] were employed.

By analyzing the results from these studies, firstly, Wu et al.[22] concluded that the errors between most experiment results and some exiting correlations including Sider-Tate's equation[29], Gnielinski's equation[30], and Hansen's equation[31] are within ±25%. This large error used to be

considered acceptable for the industry[32]. However, after reviewing developments in heat transfer, Tao[33] has pointed out that the long-accepted 20-25% error in calculating heat transfer correlations is no longer satisfactory, and an error of <10% has been going to be the new norm in recent years. Secondly, it is also found that the ranges of the salt temperature and Reynolds number (*Re*) are usually quite narrow for each experiment due to various experimental difficulties, and the common *Re* range of 10^4-10^5 for the liquid salts in energy applications was not covered. Thirdly, no reliable experiment data of Solar Salt which is the most widely-used commercial salt in CSP plants can be found in the literature. Moreover, no reliable experiment result of the flow friction has been found in the literature. Because it is very difficult to measure the pressure drop of the molten salt. On the one hand, traditional mechanical pressure gauges cannot be used because the salt can be easily frozen in the gauge. On the other hand, researchers at Sandia National Laboratories have tried to measure the pressure drop of the molten salt by using many kinds of pressure transduces[34]. However, the pressure transduces either had a failure or had a very large measuring error due to the high temperature. Finally, the receiver tubes are heated by greatly non-uniform concentrated solar irradiation flux in the CSP plant. However, it is quite difficult to do experiments under this condition. Hence, simulation approach can offer significant help investigating the flow and heat transfer features of the liquid salts[35].

In present work, two liquid fluorides (FLiNaK, NaF-$NaBF_4$)[11] that are promising for nuclear plants and two nitrates (Hitec, Solar Salt)[36] that are usually used in CSPs are considered. Both simulations and experiments are employed to investigate the heat transfer features and flow friction in round pipes. The aim of this work is as follows. Firstly, it is hard for experiments to cover the typical *Re* range of 10^4-10^5 and the whole possible salt temperature range of each salt in energy applications, so we try to use simulations to cover these ranges. Secondly, the influences of the greatly non-uniform wall flux on the flow and heat transfer characteristics will be investigated, and we try to determine if it is necessary to consider these effects in energy applications. Thirdly, the simulation heat transfer and friction data of all salts will be compared with several classical correlations to examine whether they are applicable to these liquid salts. Finally, we will try to select a heat transfer correlation from the classical equations or develop a new correlation that can achieve an error of <10% in calculating heat transfer.

2. Physical model description

2.1 A tube section from a solar receiver

An absorber tube section that is heated by the peak solar flux in the receiver of the 1 MWe DAHAN plant on spring equinox noon is taken into consideration as the physical model. The tube section is demonstrated in Fig. 1(a), and its key parameters are shown in Table 1. The studied receiver shown in Fig. 1(b) employs 620 six-meter absorber tubes[37] and can accept the concentrated solar radiation from one hundred 10m×10m heliostats[38]. The longitude and latitude of the plant that is located in Beijing are 115.9°E and 40.4°N, respectively.

For describing the model clearly, two systems of right-handed Cartesian axes are defined in Fig. 1. $X_rY_rZ_r$ is named receiver system. The origin (***A***) is the aperture center of the receiver, and the directions of the axes are shown in Fig. 1(b). $X_tY_tZ_t$ is named tube system. The origin (***O***) is the center of the tube section, and each axis is parallel to the corresponding axis in $X_rY_rZ_r$. Considering the depression angle of 25° for the receiver, the gravity vector (g) in tube system should be (0, -8.9, -4.1).

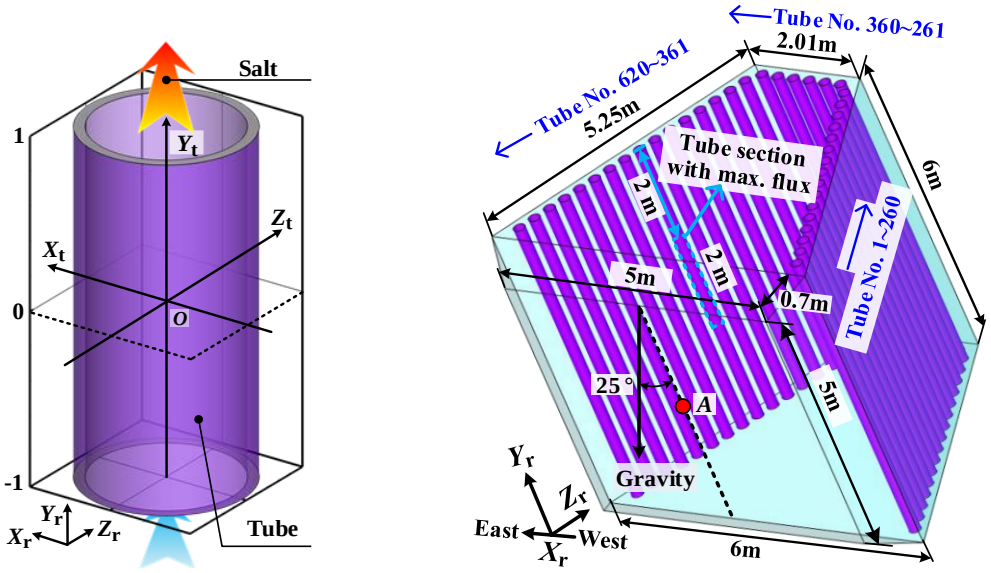

(a) Tube section of two meters (b) Solar receiver

Fig. 1. Schematics of the tube section and the solar receiver.

Table 1. Key parameters of the selected physical model[37, 39].

Items	Description or value
Material	316H stainless steel
Roughness of tube wall	hydrodynamically smooth
Inside diameter of tube D / mm	16.6
Outside diameter of tube/ mm	19
Length of tube L / mm	2000
Density of steel / $kg \cdot m^{-3}$	7090
Heat conductivity of steel / $W \cdot (m \cdot K)^{-1}$	21.5
Specific capacity of steel / $kJ \cdot (kg \cdot K)^{-1}$	0.500

2.2 Heat fluxes on tube wall and liquid salts

This work will investigate the flow features and heat transfer performance of the previously mentioned liquid salts, where the salt will flow in the two-meter tube section under uniform or non-uniform wall flux, which are described as follows.

A long-tested optical code SPTOPTIC developed in our previous work[37] using Monte Carol ray tracing (MCRT) method is employed to model the transmission of solar radiation at spring equinox noon in DAHAN plant. The MCRT is a method for calculating the paths of rays through an optical system, where possible optical events including absorption, scattering, refraction, and reflection are modeled in a random way. The MCRT has been successfully employed in the performance simulations of parabolic trough collector[40-45], linear Fresnel collector[46-49], parabolic dish collector[50-52], and solar power tower[53-56]. For simplifying the description, detailed descriptions of the model and code that has been published in Ref.[37] are omitted here.

After the simulation, a detailed contour map of the solar irradiation flux (q_l) in the liquid salt receiver is procured and presented in Fig. 2(a). Fig. 2(b) illustrates the flux absorbed on tube 443 that is heated by the peak flux of 5.14×10^5 W·m^{-2}. Fig. 2(c) depicts the greatly non-uniform solar flux absorbed by the selective absorbing coating on the studied tube section, where the total power of 11,616 W is absorbed. Furthermore, current work also tries to study the flow and heat transfer features at uniform wall flux condition, so Fig. 2(c) also illustrates a uniform flux with the value of 97,302 W·m^{-2}, which is procured by distributing the total power absorbed on the tube section uniformly on its outside wall.

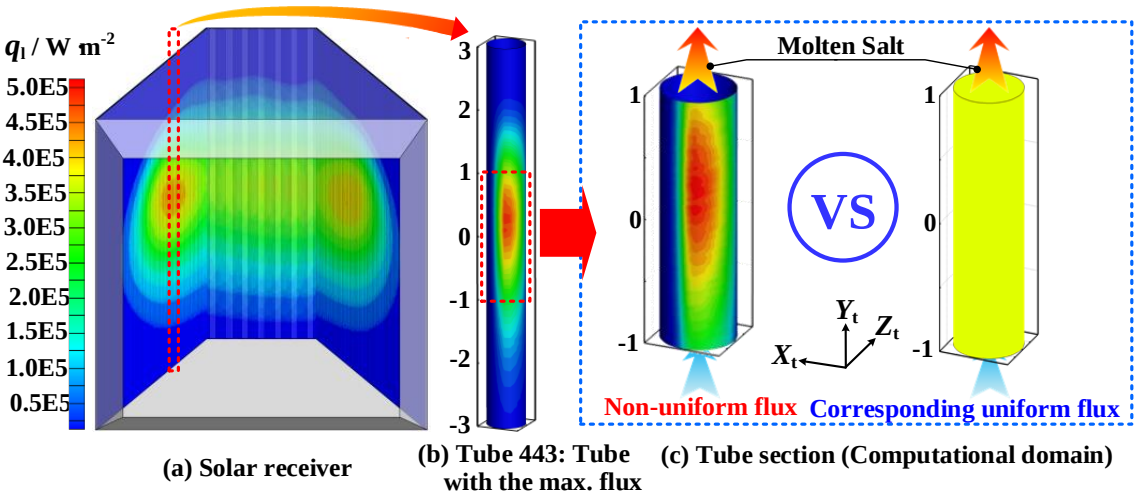

Fig. 2. Typical non-uniform and uniform heat flux distributions.

Due to the fact that a solar receiver of current dimensions can achieve a solar-thermal conversion efficiency of about 90%[57, 58]. Hence, a simplified assumption has been made by assuming that 90% of the absorbed local irradiation flux (q_l) on the tube outer wall can be transferred to the salt. And the

flux (q) calculated using Eq.(1) will be used to study the flow and heat transfer in the simulation as a heat flux boundary on the tube outer wall. After this assumption, the peak fluxes under non-uniform and uniform flux conditions would be 4.63×10^5 Wm^{-2} and 87,571 Wm^{-2}, respectively.

$$q = 0.9 \cdot q_1 \tag{1}$$

Two representative nitrates (Hitec, Solar Salt) and two representative fluorides (FLiNaK, NaF-$NaBF_4$) were considered in the current analysis. Fig. 3 illustrates the constituents and temperature-dependent thermophysical properties of the four liquid salts. Piecewise functions of these thermophysical properties are given in Table A1 in Appendix A, and were used in the simulations and experiments.

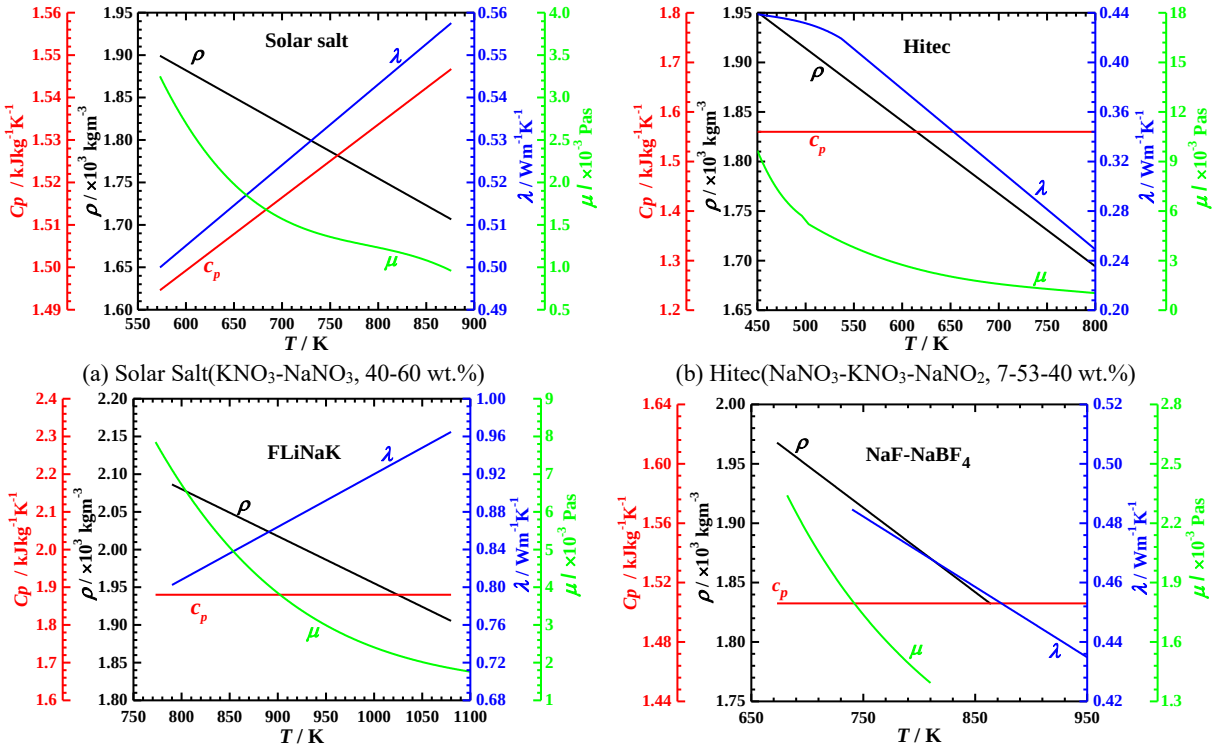

(a) Solar Salt(KNO_3-$NaNO_3$, 40-60 wt.%)

(b) Hitec($NaNO_3$-KNO_3-$NaNO_2$, 7-53-40 wt.%)

(c) FLiNaK(LiF-KF-NaF, 29.2-59.1-11.7 wt.%)

(d) NaF-$NaBF_4$(3.2-96.8 wt.%)

Fig. 3. Thermo-physical properties of the liquid salts[35, 59-61].

3. Methodology description

3.1. Modeling of heat transfer and flow in tube

For simulating the turbulent flow and heat transfer processes in the two-meter pipe section demonstrated in Fig. 1(a), the computation domain can be divided into the region of the salt and the steel region of the tube. Hexahedral meshes were generated in the two regions, and computational fluid dynamics methods were utilized to model these processes. According to the previous studies of Ferng et al.[35], Cheng et al.[62], and Chang et al.[63], the standard high-Re κ-ε model with the standard wall functions, which can predict the heat transfer and friction of the molten salts in turbulent tube flow

suitably, was selected in the current model.

3.1.1. Governing equations

Different governing equations are applied in different regions. The steel region just includes the energy equation. However, in the salt region, the mass conservation equation, the momentum equation, the standard high-Reynolds-number κ-ε equations considering the buoyancy, and the energy equation are considered and expressed in the tube system. These equations are given in Eqs.(2)-(7)[64]. The temperature-dependent thermophysical properties of the liquid salt were applied in the salt region as piecewise functions.

During the simulation, all equations were solved using ANSYS FLUENT 18.0[65]. The convective terms were discretized using second-order upwind scheme. The pressure was discretized using PRESTO! scheme. SIMPLE algorithm was used for the coupling of pressure and velocity. The convergence criteria for the continuity equation, energy equation, velocity, κ, and ε were equal to 10^{-6}.

Mass conservation equation:

$$\frac{\partial\left(\rho u_i\right)}{\partial x_i}=0 \tag{2}$$

Momentum equation:

$$\frac{\partial\left(\rho u_i u_j\right)}{\partial x_i}=-\frac{\partial p}{\partial x_i}+\frac{\partial}{\partial x_j}\left[\left(\mu_{\mathrm{t}}+\mu\right)\left(\frac{\partial u_i}{\partial x_j}+\frac{\partial u_j}{\partial x_i}-\frac{2}{3}\frac{\partial u_l}{\partial x_l}\delta_{ij}\right)\right]+\rho g_i \tag{3}$$

k and ε equations:

$$\frac{\partial\left(\rho u_i k\right)}{\partial x_i}=\frac{\partial}{\partial x_i}\left[\left(\mu+\frac{\mu_{\mathrm{t}}}{\sigma_k}\right)\frac{\partial k}{\partial x_i}\right]+G_k+G_{\mathrm{b}}-\rho\varepsilon \tag{4}$$

$$\frac{\partial\left(\rho u_i \varepsilon\right)}{\partial x_i}=\frac{\partial}{\partial x_i}\left[\left(\mu+\frac{\mu_{\mathrm{t}}}{\sigma_\varepsilon}\right)\frac{\partial \varepsilon}{\partial x_i}\right]+c_1\frac{\varepsilon}{k}\left(G_k+c_3G_{\mathrm{b}}\right)-c_2\rho\frac{\varepsilon^2}{k} \tag{5}$$

$$\mu_{\mathrm{t}}=c_\mu\rho\frac{k^2}{\varepsilon},G_k=\mu_t\frac{\partial u_i}{\partial x_j}\left(\frac{\partial u_i}{\partial x_j}+\frac{\partial u_j}{\partial x_i}\right),G_{\mathrm{b}}=\beta g_i\frac{\mu_{\mathrm{t}}}{Pr_{\mathrm{t}}}\frac{\partial T}{\partial x_i} \tag{6}$$

Energy equation:

$$\frac{\partial\left(\rho u_i h\right)}{\partial x_i}=\frac{\partial}{\partial x_i}\left[c_p\left(\frac{\mu}{Pr}+\frac{\mu_{\mathrm{t}}}{Pr_{\mathrm{t}}}\right)\frac{\partial T}{\partial x_i}\right] \tag{7}$$

where c_1=1.44, c_2=1.92, c_μ=0.09, σ_k=1.0, σ_ε=1.3; $c_3=\tanh\left|v_{\mathrm{p}}/v_{\mathrm{n}}\right|$. v_{p} and v_{n} are the components of the fluid velocity vector. They are parallel and perpendicular to the vector of the acceleration of gravity (g), respectively.

3.1.2. Near-wall treatments

It is known that the near-wall region can be divided into three layers. The closest layer to the wall is called viscous sublayer, where the flow is almost laminar, and the molecular viscosity plays a dominant role. The layer next to the viscous sublayer is called buffer layer, where the effects of molecular viscosity and turbulence are both important. The farthest layer from the wall is called fully-turbulent layer, where turbulence plays a dominant role.

Because the high-*Re* k-ε model is inapplicable in the viscous sublayer and buffer layer, semi-empirical formulas called "wall functions" can be used to bridge these layers between the wall and the fully turbulent region[65]. For the region near the tube inner wall, a logarithmic law is employed, which states that the average velocity of a turbulent flow at a certain point (P) in the fully-turbulent layer is proportional to the logarithm of the distance from that point to the wall, as shown in Eq.(8) [65]. Moreover, the logarithmic law is known to be valid for $30<y^+<500$[66]. Although, ANSYS FLUENT suggests that the lower limit of y^+ always lies in the order of ~15[65]. Below this limit, wall functions will typically deteriorate and the accuracy of the solutions cannot be maintained. In the current simulation, to ensure that the logarithmic law is valid, y+ of the near-wall node is kept within 30-60 by modifying the mesh case by case.

$$\begin{aligned} u^+ &= \frac{1}{\kappa}\ln\left(E\cdot y^+\right) \\ u^+ &= \frac{u_{\mathrm{P}}\cdot c_\mu^{0.25}\cdot k_{\mathrm{P}}^{0.5}}{\tau_{\mathrm{w}}/\rho} \\ y^+ &= \frac{\rho\cdot c_\mu^{0.25}\cdot k_{\mathrm{P}}^{0.5}\cdot y_{\mathrm{P}}}{\mu} \end{aligned} \tag{8}$$

where κ is von Kármán constant (= 0.4187); E is an empirical constant (= 9.793); u_{P} is the mean velocity of the fluid at the near-wall node; k_{P} is the turbulence kinetic energy at the near-wall node; y_{P} is the distance from point to the wall.

Reynolds' analogy between momentum and energy transport gives a similar logarithmic law for

199 mean temperature at the near-wall node P, as shown in Eq.(9)[65].

$$T^+ = \frac{\left(T_\mathrm{w} - T_\mathrm{P}\right)\rho c_p \cdot c_\mu^{0.25} \cdot k_\mathrm{P}^{0.5}}{q_\mathrm{w}}$$

200
$$= \begin{cases} Pr \cdot y^+ + 0.5\rho Pr \dfrac{c_\mu^{0.25} \cdot k_\mathrm{P}^{0.5}}{q_\mathrm{w}} u_\mathrm{P}^2, y^+ < y_\mathrm{T}^+ \\ Pr_\mathrm{t}\left[\dfrac{1}{\kappa}\ln\left(E \cdot y^+\right) + P\right] + \\ 0.5\rho \dfrac{c_\mu^{0.25} \cdot k_\mathrm{P}^{0.5}}{q_\mathrm{w}}\left[Pr_\mathrm{t} u_\mathrm{P}^2 + \left(Pr - Pr_\mathrm{t}\right)u_\mathrm{c}^2\right], y^+ \geq y_\mathrm{T}^+ \end{cases} \tag{9}$$

$$P = 9.24\left[\left(\frac{Pr}{Pr_\mathrm{t}}\right)^{0.75} - 1\right]\left[1 - 0.28 \cdot e^{-0.007 Pr/Pr_\mathrm{t}}\right]$$

201 where T_w is the temperature at the wall; T_w is the temperature at the first near-wall node P; q_w is the
202 wall heat flux. A constant Pr_t assumption of 0.85 that were employed in Refs.[35, 62, 63] was used in
203 the current model, because the variation of Pr_t influences little on the heat transfer and flow of the salt.

204 The production of k (G_k) at the near-wall cell is based on the logarithmic law and can be computed
205 using Eq.(10), and ε can be computed using Eq.(11) [65].

206
$$G_k \approx \tau_\mathrm{w}\frac{\partial u}{\partial y} = \tau_\mathrm{w}\frac{\tau_\mathrm{w}}{\kappa\rho \cdot c_\mu^{0.25} \cdot k_\mathrm{P}^{0.5} \cdot y_\mathrm{P}} \tag{10}$$

207
$$\varepsilon_P = \tau_\mathrm{w}\frac{c_\mu^{0.75} \cdot k_\mathrm{P}^{1.5}}{\kappa \cdot y_\mathrm{P}} \tag{11}$$

208 **3.1.3. Boundary conditions**

209 Different boundary conditions were applied on the boundaries of the computational domain[65].

210 (1) At the inlet of the salt region, constant temperature($T_\mathrm{f,in}$) and constant velocity ($u_\mathrm{f,i}$) were used.
211 The turbulent kinetic energy at the inlet ($k_\mathrm{f,i}$) was estimated using $k_\mathrm{f,i} = 1.5\left(u_\mathrm{f,i} I_\mathrm{f,i}\right)^2$. The
212 turbulent dissipation rate at the inlet ($\varepsilon_\mathrm{f,i}$) was estimated using $\varepsilon_\mathrm{f,i} = c_\mu^{0.75} k_\mathrm{f,i}^{1.5} / \left(0.07D\right)$.
213 $I_\mathrm{f,i} = 0.16 \cdot Re^{-0.125}$ is the turbulence intensity at the inlet.

214 (2) For the outlet of the salt region, the fully developed condition was utilized. $\partial\phi/\partial x = 0$,
215 where ϕ represents the velocity, k, ε, and temperature.

216 (3) At the tube's inner surface, a coupled boundary for the temperature and no-slip interface for

217 the velocity were used.

218 (4) At the tube wall ends, an adiabatic boundary was considered: $q_w = 0$.

219 (5) At the outside surface of the tube, a heat flux boundary was employed, where the uniform or
220 non-uniform wall heat flux described in Section 2.2 was considered.

221 **3.2. Experiments of heat transfer in tube side of a STHX**

222 For a specific fluid, many previous studies have concluded that the performance of heat transfer
223 in a pipe under uniform wall flux is almost the same as that in the tubes of a STHX[32]. As a result, the
224 computation model can be validated by comparing the simulation heat transfer results procured using
225 uniform wall flux and the experiment data procured in the tubes of a STHX, where Hitec is employed
226 as the heat transfer fluid. The details of the experiment are as follows.

227 Table 2 presents the key parameters of the heat exchanger. A tube bundle with nineteen tubes is
228 assembled in a shell with an inside diameter of 100 mm as illustrated in Fig. 4, and each tube has an
229 effective length of 2.0 m. A 150 mm aluminum silicate layer is employed to cover the exchanger for
230 reducing the thermal loss to a negligible level.

231 Table 2. Geometric parameters of the STHX.

Parameter / unit	Value
Shell's outside diameter / mm	108
Shell's inside diameter / mm	100
Arrangement of tubes	regular triangle
Number of tubes	19
Tube pitch / mm	18
Length of each tube / m	2.0
Tube's outside diameter / mm	14
Tube's inside diameter / mm	10

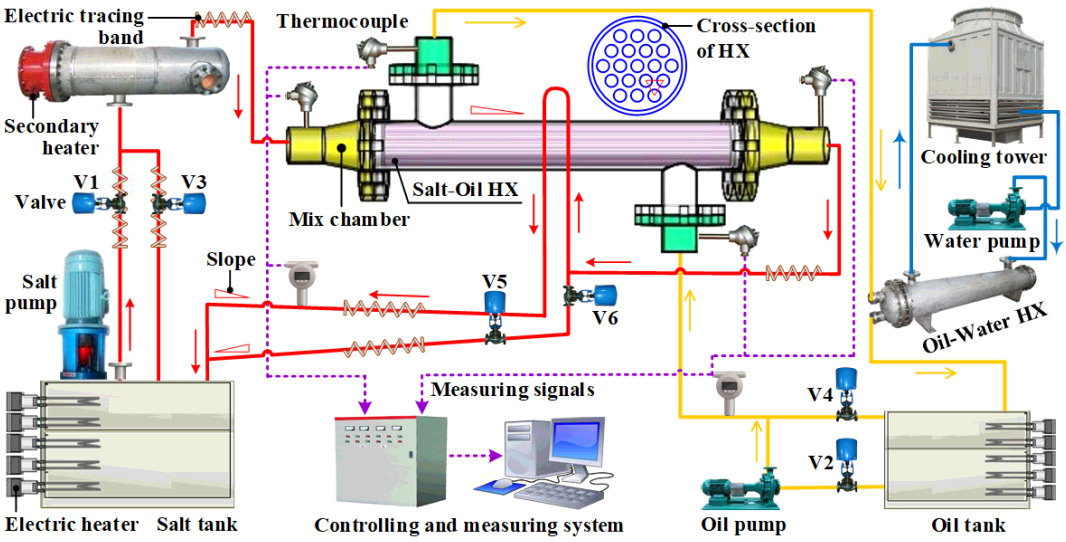

Fig. 4. Sketch of the experiment system.

A liquid salt experiment system demonstrated in Fig. 4 was built to investigate the heat transfer of Hitec in the tubes of the STHX. The system consists of a liquid salt path, a synthetic oil path, and a cooling path.

In the liquid salt path, a molten salt tank with electric heaters is employed to contain and heat the Hitec of 6 tons. A pump is used to pump the liquid Hitec throughout this path. A secondary electric heater is used to adjust the salt temperature at the tube inlet of the salt-oil HX. The volume flow rate of Hitec is measured using a vortex shedding flow gauge. For the horizontal connecting pipes, an inclination angle of about 5° is specially designed to ensure that the Hitec can flow back to the tank. All connecting pipes are heated using electric tracing bands to avert the solidification of liquid salt. To ensure that the tube side can be fully filled, an invert U-shaped connecting pipe was installed at the outlet of this side. The synthetic oil path uses a tank to store two-ton YD-325 synthetic oil whose thermophysical properties are summarized in Table A1. A pump is used to pump the oil throughout this path including the shell-side passage in the salt-oil HX. The volume flow of the oil is also measured with a vortex shedding flow gauge. In addition, the cooling path includes a water-cooling tower, a pump, and the shell-side passage of the oil-water HX.

During the experiment, the valve V1 and Valve V2 must keep open, while other valves should be closed. Moreover, the pumps should be launched. The energy transfer processes are as follows. Firstly, the thermal energy will be exchanged to the synthetic oil from the liquid Hitec within the testing salt-

oil HX. Secondly, the energy will be transferred to the cooling water through the water-oil exchanger. At last, the cooling tower would release the energy to the surrounding air. The two flow gauges have the relative uncertainty of 1.0%. K-type thermocouples employed in the temperature measurement have the uncertainty of 0.5K. In the test, the salt temperature ranges from 523K to 573K, while the temperature of the oil varies between 373K and 413K. The oil volume rate of flow is 20.0 m^3h^{-1} and remains unchanged. All heat transfer data are within the thermal balance deviation of 7%.

After the experiment, the Nusselt number (*Nu*) and convective heat transfer coefficient of Hitec were procured using the Wilson plot method proposed in Ref.[67]. The uncertainties of the experiments are examined using the approach of Coleman and Steele [68], which indicates that the overall heat transfer coefficient, the *Re* number, and *Nu* number have the uncertainties of ±3.5%, ±1.8%, and ±7.2%, respectively. The above two methods which have been widely used in previous work and introduced clearly in Refs.[67, 68] are omitted here to simplify the description.

3.3. Parameter definitions

Several performance parameters which will be employed to characterize the flow and heat transfer features in tube are introduced as follows. Equation (12) defines the Reynolds number(*Re*), the convective heat transfer coefficient(*h*) and the Nusselt number(*Nu*). Equation (13) defines the friction factor (*f*) of liquid flow. Equation (14) defines the velocity(v_f) and the qualitative temperature(T_f) of the salt. Equation (15) defines the logarithmic mean temperature difference (ΔT) between inner wall of the tube and the salt.

$$Re = \frac{\rho D v_f}{\mu}, h = \frac{Q}{A\Delta T}, Nu = \frac{hD}{\lambda} \tag{12}$$

$$f = \Delta p \cdot \frac{D}{L} \frac{1}{(1/2)\rho v_f^2} \tag{13}$$

$$v_f = \frac{m}{\rho A_c}, T_f = \left(T_{f,o} + T_{f,i}\right)/2 \tag{14}$$

$$\Delta T = \left(T_{f,o} - T_{f,i}\right) \Big/ \ln \frac{\left(T_w - T_{f,i}\right)}{\left(T_w - T_{f,o}\right)} \tag{15}$$

$$T_{f,i} = \frac{\int_{A_c} T \cdot c_p \rho v dA}{\int_{A_c} c_p \rho v dA}, T_{f,o} = \frac{\int_{A_c} T \cdot c_p \rho v dA}{\int_{A_c} c_p \rho v dA} \tag{16}$$

where λ represents the heat conductivity; μ represents the dynamic viscosity; Q represents the power

converted to the salt; Δp indicates the drop of pressure from the inlet to the outlet; A is heat transfer area; L represents the length of the tube; T_w represents the average temperature of heat transfer surface; A_c represents the area of the inlet or outlet; $T_{f,o}$ and $T_{f,i}$ represent the salt temperatures at the tube's outlet and inlet, respectively.

4. Model validation

The numerical model was validated in the following way. Firstly, an independence check of the mesh was carried out to eliminate its possible influences on the computation. Secondly, the numerical results of the water were compared with some classical correlations. Finally, the numerical results of Hitec and FLiNaK were compared with corresponding experimental data, respectively.

4.1 Mesh independence check

In the simulation, the effects of the mesh on the results should be eliminated for each case. An example was used to illustrate the mesh independence check as follows. Firstly, different hexahedral mesh systems were generated, where the mesh in the axial direction is uniform. Then, the flow and heat transfer for the Hitec were simulated under non-uniform flux for each mesh system, where the typical condition of $u_{f,i}$=4 ms^{-1} and $T_{f,i}$=650K were considered. Then, the simulated Nu number and f number for these mesh systems were compared as shown in Fig. 5. It is seen the variations of Nu number and f number are less than 0.23% and 0.08% when the mesh number increases from 1680×250 (cross-section×axial) to 3317×300, respectively. Considering the computational accuracy and time, the mesh system of 1680×250 can be found to be adequate for the current case, where y^+=30.7-45.5.The cross-section of this mesh system is shown in Fig. 6. For other cases simulated in current work, mesh independence check has also been conducted in a similar way.

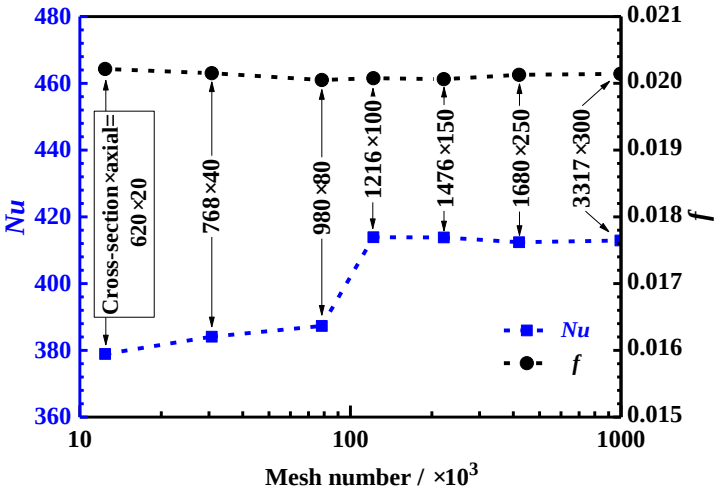

Fig. 5. Mesh independence test using several mesh systems (cross-section × axial).

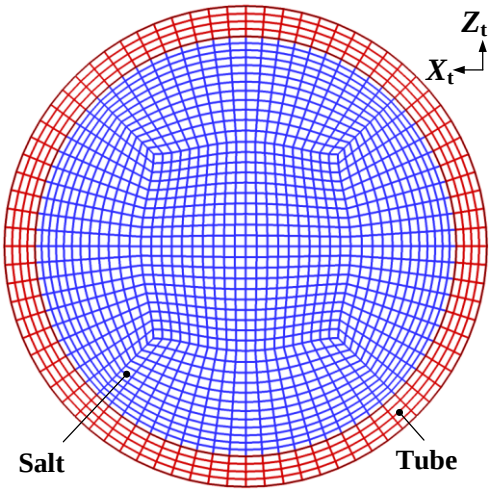

Fig. 6. Cross-section of the typical mesh that is uniform in axial direction.

4.2 Validation of the model for water

It is known that the *Nu* number and *f* number of water can be described well by the classical Gnielinski's[30] and Filonenko's[69] correlations, respectively. For ensuring that current simulation methods is suitable and accurate for modeling the heat transfer in turbulent tube flow, the simulated results of *Nu* and *f* were compared with the predicted data from the above classical correlations as shown in Fig. 7, where $T_{f,i}$ =300K. It is observed that the simulated results agree quite well with the correlations when Re=10^4-10^5. The differences between the simulated *Nu* numbers and the Gnielinski's correlation are within ±3.5%, and corresponding differences for *f* number are smaller than 1.3%. The above results indicate that current simulation methods and model are suitable and quite accurate for simulating the turbulent flow and heat transfer in a tube.

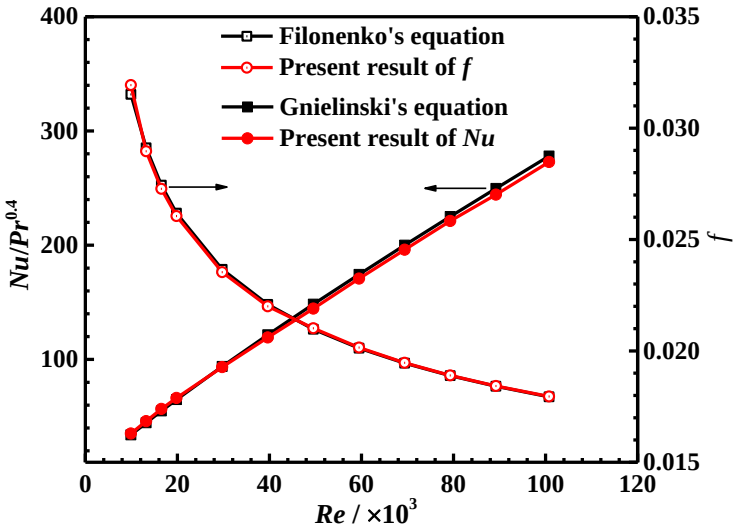

Fig. 7. Comparison between numerical results and classical correlations of water.

4.3 Validation of the model for Hitec

The heat transfer performance of Hitec was simulated under uniform wall flux in turbulent tube flow, where T_f was kept at around the average salt temperature in the experiment, i.e., 550K. The comparison of the numerical and experimental results is shown in Fig. 8. It can be observed that the numerical result agree quite well with the experimental data in the whole range of *Re*, and the average differences under different *Re* are within ±4%. Most importantly, it can be seen that all simulation data are within the error bars of the experimental data. It indicates that the model is reliable for simulating the heat transfer of Hitec in the tube.

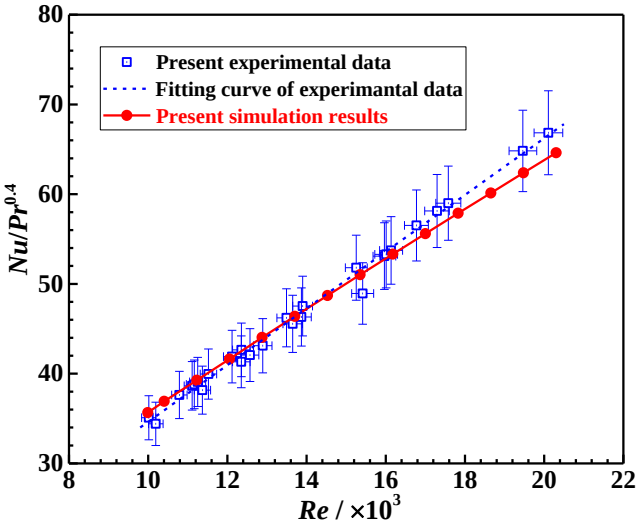

Fig. 8. Comparison between numerical and experimental results of Hitec.

4.4 Validation of the model for FLiNaK

For FLiNaK, the simulation was conducted under different *Re* when T_f was around 898K which is the average temperature of the salt in the experiments of Vriesema[19]. In the experiments, the salt flowed in the tube side of a concentric tube exchanger, and air flowed in the shell side. The salt inlet temperature was in the range of 848K-948K in the test. The modeling results are compared with the testing data of Vriesema[19] as shown in Fig. 9, where Ferng et al.'s simulation data[35] are also shown. It is seen that the current numerical results which are similar to Ferng et al.'s results[35] agree well with the experimental data, and the average deviations are smaller than ±5%, which indicates that the model is accurate for modeling the heat transfer of FLiNaK in the tube.

To sum up, the above comparisons indicate that the current model is reliable for simulating the heat transfer of the fluoride and nitrate in turbulent tube flow.

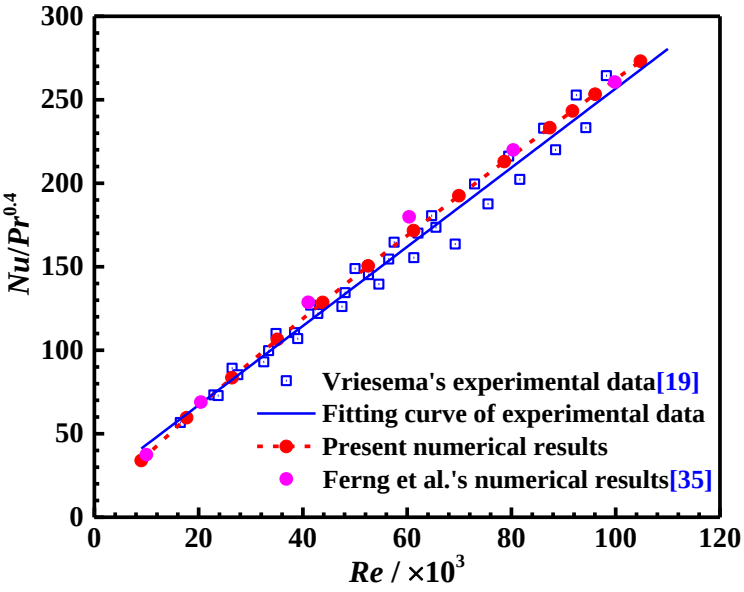

Fig. 9. Comparison between numerical and experimental results of FLiNaK.

5. Results and discussion

In the following section, firstly, influences of the extreme non-uniform heat flux would be examined. Then, simulations are employed to extend the temperature and Reynolds number to large ranges that cannot be easily achieved in experiments. The simulation results of all salts will be compared with some classical correlations for checking whether they are applicable to the salts. Finally, we would try to select or develop a heat transfer correlation that can achieve an error of <10%.

5.1. Heat transfer and friction under uniform and non-uniform fluxes

5.1.1 Influences of flux uniformity on temperature and velocity

Hitec is taken as the example to study the effects of the non-uniform and uniform fluxes on the distribution of the temperature on the tube, where $u_{f,i}$=4 ms^{-1}, $T_{f,i}$=650K. Fig. 10(a) shows the non-uniform temperature whose profile is similar to the non-uniform heat flux in Fig. 2 (c). And the hotspot region is at the position that absorbs the peak flux. Furthermore, it is observed in Fig. 10(b) the outlet of the tube is the hottest region under uniform heat flux. This is due to the fact that the salt is gradually heated from tube inlet to its outlet, and the temperature of the tube also keeps on rising. In addition, it can be observed that the peak temperature for the non-uniform heat flux is 66 K higher than that under uniform heat flux. It is well-known that the local hot region can result in serious adverse effects, such as the salt decomposition, corrosion of the tube, and stress failure. Thus, the operation condition should be monitored and controlled carefully to avert possible overheating in solar receivers.

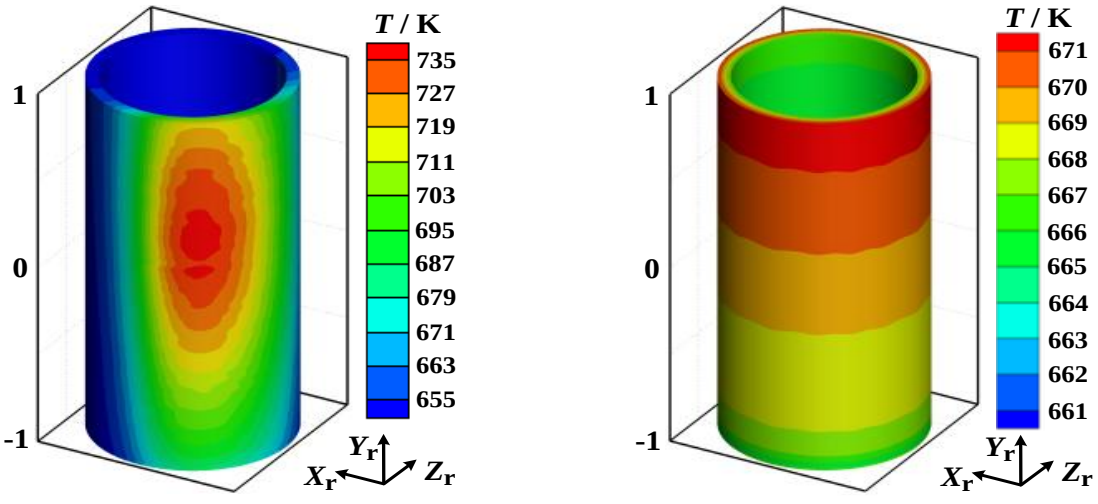

(a) Under non-uniform heat flux, T_{max}=738.0 K. (b) Under uniform heat flux, T_{max}=672.0 K.

Fig. 10. Temperatures of the tube under different flux distributions when Hitec is used.

Fig. 11 shows the typical distributions of the Hitec temperature and velocity magnitude at the middle cross section (Y_t=0) under non-uniform and uniform fluxes, where $u_{f,i}$=4 ms^{-1}, $T_{f,i}$=650K. It is

seen that the temperature under non-uniform flux is quite non-uniform with a hot region at the lower half as shown in Fig. 11(a), where the maximum temperature difference in the cross section is around 13.5K. In Fig. 11(b), it is observed that the temperature shows an axisymmetric pattern, and the maximum temperature difference is 5.7K. Moreover, it is seen in Fig. 11(c)(d) that the velocity distributions under the two flux distributions also show axisymmetric features, and they are quite similar to each other, which indicates that the flux distribution has no significant influence on the velocity distribution. However, it can be found that the peak velocity under non-uniform flux is slightly higher than that under uniform flux by comparing the values of velocity in Fig. 11(c) and (d). This should be a result of the slightly larger buoyancy caused by the larger temperature difference and the gravity(g) under non-uniform flux, as shown in Fig. 11(a).

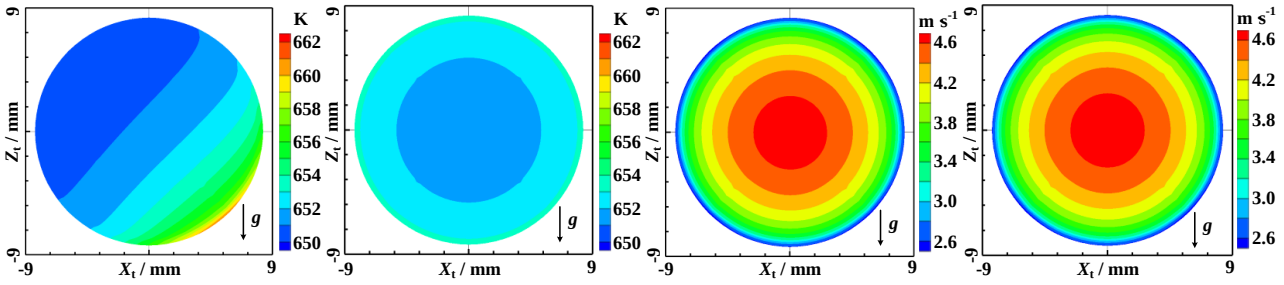

(a) Temperature, non-uniform flux (b) Temperature, uniform flux (c) Velocity magnitude, non-uniform flux (d) Velocity magnitude, uniform flux

Fig. 11. Temperatures and velocity magnitude of the Hitec under different flux distributions at Y_t=0.

5.1.2 Influences of flux uniformity on heat transfer performance

Influences of the uniform and non-uniform fluxes on the heat transfer features of the liquid salts would be examined in this part. For every liquid salt, the broadest possible range of the temperature would be considered under a typical inlet velocity.

Fig. 12 illustrates the performance of heat transfer for every salt at both non-uniform and uniform heat fluxes. It is observed that Re number for every liquid salt rises with the increase of temperature at the same velocity. This is due to the variations of the density and dynamic viscosity with the temperature as shown in Fig. 3. Moreover, it is found that the values of $Nu/Pr^{0.4}$ at non-uniform wall flux for every salt are about 2% higher than those with uniform wall flux at different temperatures. This phenomenon is caused by the hot region, which is at the bottom of the tube section, under non-uniform wall flux, as

shown in Fig. 10(a) and Fig. 11(a). This hot region can introduce slightly stronger buoyancy in the liquid salt than that with uniform wall flux, which can strengthen the heat transfer performance between the tube wall and the liquid salt slightly.

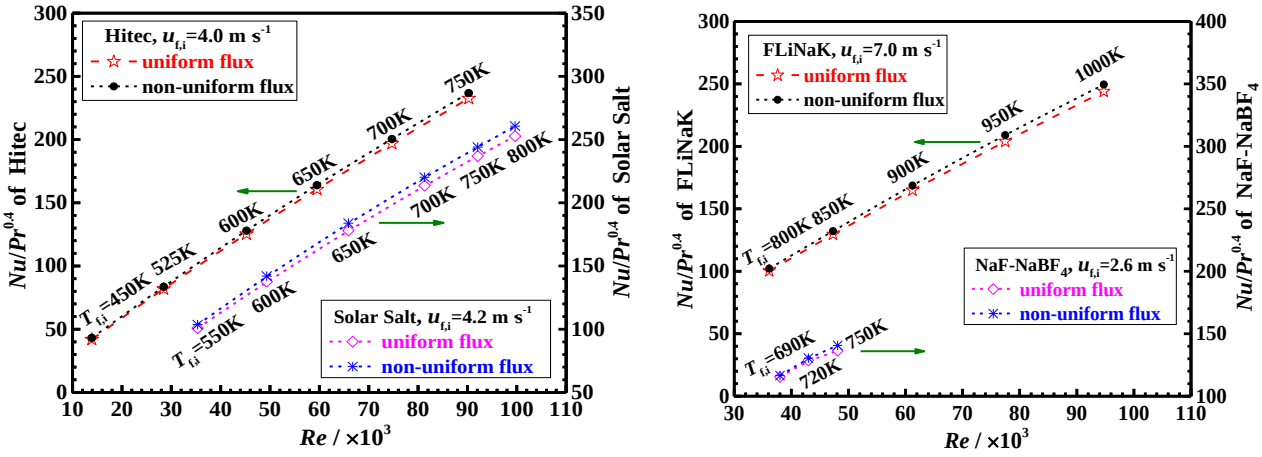

(a) Nitrates: Hitec, Solar Salt (b) Fluorides: FLiNaK, NaF-NaBF$_4$

Fig. 12 Heat transfer performance under non-uniform and uniform heat fluxes.

5.1.3 Influences of flux uniformity on friction coefficient in tube

The influences of the flux distributions on the friction characteristics of the four liquid salts are examined in this part, where the temperature range of each salt is the same as that in the above section. Fig. 13 presents the friction factors (f) of each salt under both non-uniform and uniform wall fluxes. It can be found that no obvious difference is observed between the friction factors of each salt at non-uniform and uniform wall fluxes at different temperatures, and the errors are within ±0.5%. This phenomenon indicates that the effect of the flux uniformity on the flow friction is inappreciable.

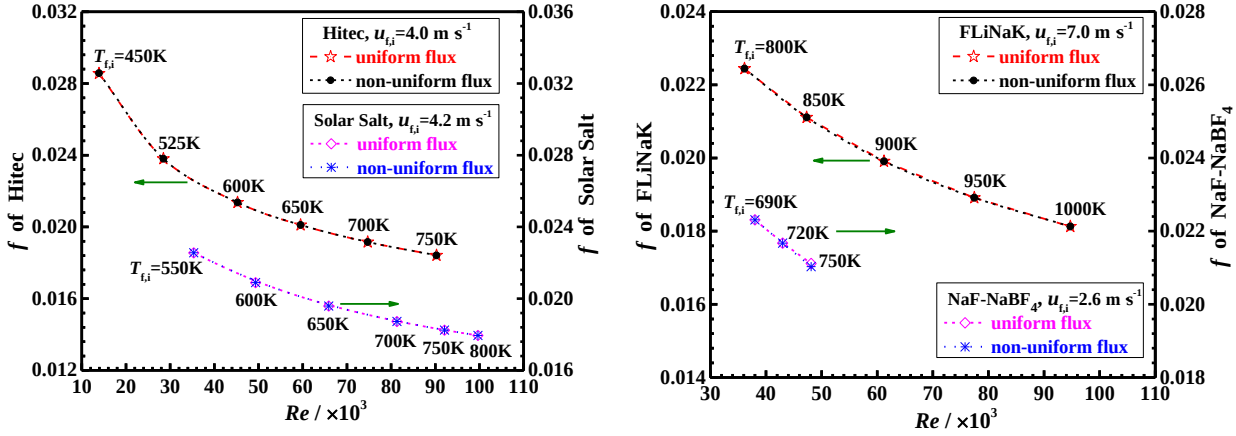

(a) Nitrates: Hitec, Solar Salt (b) Fluorides: FLiNaK, NaF-NaBF$_4$

Fig. 13. Friction factors under non-uniform and uniform heat fluxes.

After the above examinations, it can be found the non-uniform heat flux influences the tube temperature obviously, but the effects on both heat transfer and friction factor are negligible. These facts offer an important suggestion that it is unnecessary to use experiments, which are complex, tough and expensive, to obtain the heat transfer and friction correlations under non-uniform heat flux, because the correlations should be very close to those under uniform heat flux. In addition, the studied non-uniform flux is a typical extreme condition in the industry, and the fluxes under other conditions in the industry usually cannot be more non-uniform than the current case. As a result, due to the fact that the current non-uniform flux influences little on heat transfer and friction, it can be inferred that similar phenomenon can be found under other non-uniform flux conditions in the industry.

In the rest of this work, the flow friction and heat transfer features will just be studied using uniform heat flux, but the procured correlations should also be applicable under non-uniform flux.

5.2. Comparison of simulated data and classical correlations

Some classical correlations including Gnielinski's equation given in Eq.(17) [30], Hausen's correlation given in Eq.(18) [31], and Sider-Tate's correlation shown in Eq.(19) [29] can calculate the heat transfer performance of ordinary fluids in tube appropriately. Moreover, the Filonenko's correlation shown in Eq.(20) also can calculate the friction factor of ordinary fluids accurately.

$$Nu=0.012\left(Re^{0.87}-280\right)Pr^{0.4}\left(\frac{Pr_{\mathrm{f}}}{Pr_{\mathrm{w}}}\right)^{0.11}\left[1+\left(\frac{D}{L}\right)^{2/3}\right] \tag{17}$$

Pr=0.6-10^5, Re=2300-10^6

$$Nu=0.037\left(Re^{0.75}-180\right)Pr^{0.42}\left(\frac{\mu_{\mathrm{f}}}{\mu_{\mathrm{w}}}\right)^{0.14}\left[1+\left(\frac{D}{L}\right)^{2/3}\right] \tag{18}$$

Pr=0.5-1000, Re=2300-10^6

$$Nu=0.027Re^{0.8}Pr^{1/3}\left(\frac{\mu_{\mathrm{f}}}{\mu_{\mathrm{w}}}\right)^{0.14} \tag{19}$$

Re>10^4, Pr=0.7-16700, L/D>60

$$f=\left(1.82\lg Re-1.64\right)^{-2} \tag{20}$$

Pr=0.6-10^5, Re=2300-10^6

In this part, the simulation data of heat transfer performance and flow friction are used to compare with the above classical equations for examining if these equations are still appropriate for the liquid salts. In the simulation, the Re number covers a wide range of 10^4-10^5. The examined ranges of the bulk temperature for the four salts are given in Table 3, which is determined after considering that the highest temperature of each salt will be within the reliable temperature range of its thermophysical properties.

Table 3. The ranges of bulk temperature for the liquid salts.

Liquid salt	$T_{f,i}$ / K	T_f / K
Solar Salt	600~800	600~830
Hitec	450~700	450~722
NaF-$NaBF_4$	690~750	691~778
FLiNaK	800~1000	800~1009

5.2.1 Numerical heat transfer results versus Gnielinski's correlation

A comparison between the simulated results of the heat transfer performance for the four liquid salts and Gnielinski's correlation is shown in Fig. 14. It can be observed that the values predicted for the four salts by the Gnielinski's correlation are generally higher than the simulation data. For the nitrate salts, the maximum error between the simulated results and the correlation is about -15%. For the fluorides, the maximum error is around -10%. Moreover, it is found that simulation heat transfer data of each salt drops with decreasing salt temperature at the same *Re* number.

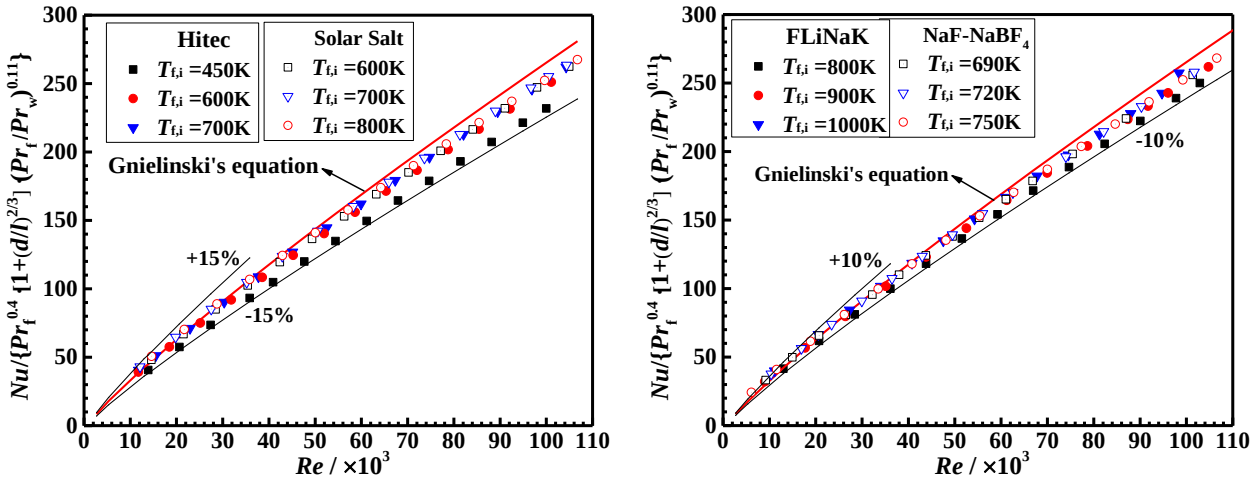

(a) Nitrates: Hitec, Solar Salt (b) Fluorides: FLiNaK, NaF-$NaBF_4$

Fig. 14. Simulation data of heat transfer versus Gnielinski's correlation.

5.2.2 Numerical heat transfer results versus Hausen's correlation

A comparison between the simulated results of the heat transfer performance and Hausen's correlation is illustrated in Fig. 15. It can be found that the numerical data are generally larger than the values predicted by Hausen's correlation. For each salt, it can be observed the error between the simulated results and Hausen's correlation rises with the increasing temperature at the same Reynolds number. The largest error of the four salts can reach +25%.

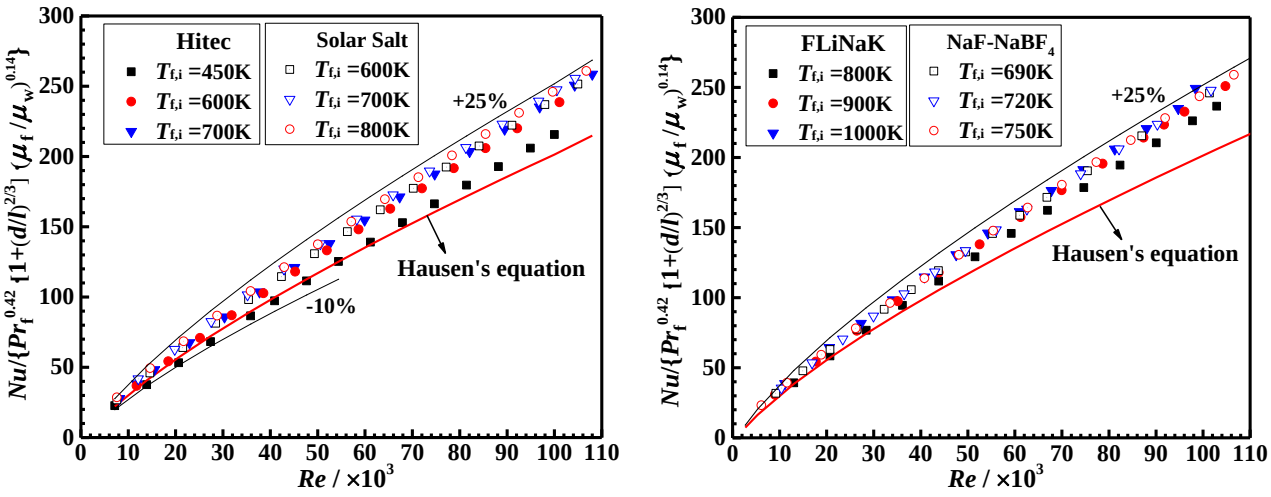

(a) Nitrates: Hitec, Solar Salt (b) Fluorides: FLiNaK, NaF-NaBF$_4$

Fig. 15. Simulation data of heat transfer versus Hausen's correlation.

5.2.3 Numerical heat transfer results versus Sider-Tate's correlation

A comparison between the simulated results of the heat transfer performance and Sider-Tate's correlation is demonstrated in Fig. 16. It can be seen in Fig. 16 that the numerical results of all the salts are generally higher than the values estimated by Sider-Tate's correlation. Moreover, the errors between the simulation results and Sider-Tate's correlation are in the range of -5% - +13%, which is relatively small.

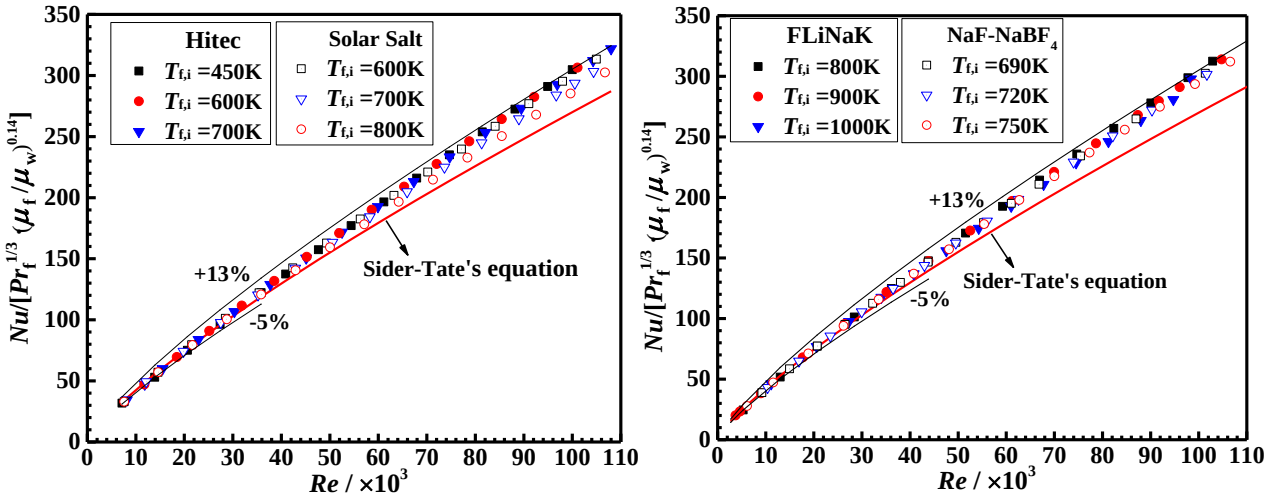

(a) Nitrates: Hitec, Solar Salt (b) Fluorides: FLiNaK, NaF-NaBF$_4$

Fig. 16. Simulation data of heat transfer versus Sider-Tate's correlation.

After summarizing the above results, it can be found that Hausen's correlation is not accurate enough, especially under relatively low temperature for Hitec, and the largest error between the

simulated results and Hausen's correlation can reach +25%. As a result, Hausen's correlation should be inappropriate for calculating the performance of heat transfer for liquid salts. Meanwhile, it is also found that the Sider-Tate's equation and Gnielinski's equation can predict the performance of the liquid salts more accurately, and the biggest errors are around +13% and -15%, respectively. These errors used to be considered acceptable for the industry[32]. However, after reviewing developments in heat transfer, Tao[33] pointed out that an error of <10% has been going to be the new norm in recent years, which is significant for enhancing the performance, reducing heat exchanger's volume and cost.

5.2.4 Numerical friction factor versus Filonenko's correlation

A comparison between the numerical friction factor(*f*) and the Filonenko's correlation is demonstrated in Fig. 17. It is seen that the simulated results of the friction factors for the four liquid salts under all modeling conditions agree excellently well with this correlation. All numerical data points are within the error of ±2% of the correlation. This result indicates that the Filonenko's correlation is suitable for predicting the friction factors of all the four liquid salts.

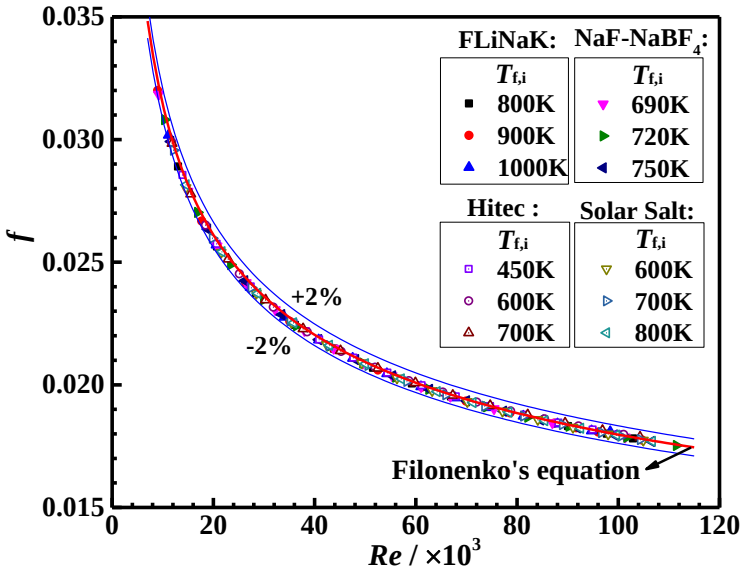

Fig. 17. Simulated friction factor(*f*) versus Filonenko's correlation.

5.3. A new heat transfer correlation proposed for the liquid salts

To predict the heat transfer performance better, the simulated data procured under a wide range of *Re* number and the broadest possible ranges of the temperature for the four liquid salts as given in Table 3 are employed to develop a new correlation, which is shown in Eq.(21). A comparison between the new correlation and the simulated data is demonstrated in Fig. 18, which indicates that the new correlation is excellently coincident with all simulated results. The largest relative error of the simulated results and the developed correlation is smaller than ±5%. In addition, the errors for 95% data points

are smaller than ±3%.

$$Nu=0.0154\cdot Re^{0.853}\cdot Pr^{0.35}\cdot\left(\frac{\mu_f}{\mu_w}\right)^{0.14} \tag{21}$$

where $\mu_f/\mu_w=1.01-1.30$; $Re=10^4-10^5$; $Pr=3.3-34$.

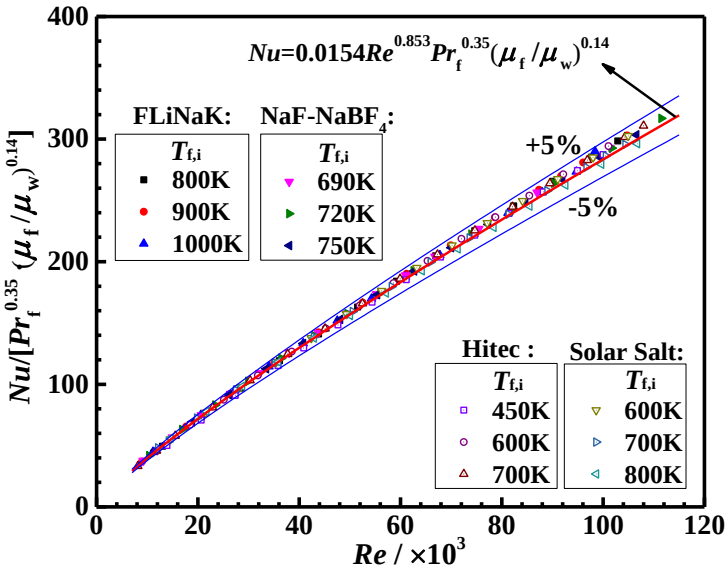

Fig. 18. New heat transfer correlation versus simulated data of the four liquid salts.

Finally, a comparison between the developed correlation and some experimental results of three representative liquid salts is illustrated in Fig. 19. In the comparison, Silverman's experiment data of NaF-NaBF4[15] , Vriesema's experiment data of FLiNaK[19], and current experiment data of Hitec are taken into account. The comparison demonstrates that all the experiment results are well coincident the developed correlation. It is found that the errors between 80% experiment data and present correlation are smaller than ±5%. Moreover, the errors between 90% experiment data and the new correlation are found to be within ±10%. The results manifest that current correlation can predict the performance of heat transfer for the four liquid salts accurately in turbulent tube flow, which can meet the requirements of high accurate correlations in the design of energy systems and help to reduce the cost of investment.

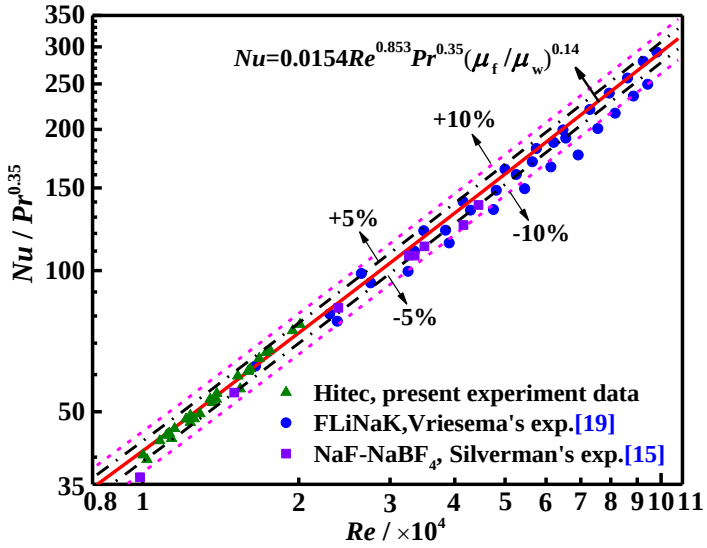

Fig. 19. New heat transfer correlation versus the experiment results of three typical salts.

6. Conclusions

The heat transfer capability and friction features for representative liquid salts employed in energy applications are investigated under the turbulent condition in a tube with wide ranges of velocity and temperature, where four liquid salts including Hitec, Solar Salt, NaF-$NaBF_4$, and FLiNaK are studied. The following conclusions are obtained.

(1) A computational model was developed to simulate the flow and heat transfer processes of the liquid salts, and experiments were conducted to test the heat transfer capability of Hitec when it flows in the tube side of a STHX. Comparing the modeled results of Hitec and the experiment results indicates that the average differences are smaller than ±4%, which manifests that the modeling method is reliable, and the simulation model is believable.

(2) Examination of the influences of the flux uniformity on flow and heat transfer indicates that the non-uniform wall flux can lead to local hotspot but influences little on the friction factor and heat transfer performance comparing with those under uniform flux. This fact suggests that the friction and heat transfer correlations acquired with uniform wall flux are applicable under non-uniform flux. So, it is unnecessary to further use experiments, which are expensive and tough, to obtain the correlations under non-uniform.

(3) Comparisons between the simulated results procured within wide velocity range and temperature interval and some exiting correlations were carried out. Hausen's correlation is found to be not suitable for the salts with a maximum error of +25%. While Sider-Tate's correlation and Gnielinski's correlation are relatively accurate with the biggest errors of +13% and -15%, respectively. In addition, Filonenko's correlation could predict the friction factor in a quite accurate way with the maximum error of ±2%.

(4) To predict the heat transfer capability for the four representative liquid salts more accurately under broad ranges of *Re* number and temperature, a correlation was proposed, where $\mu_f/\mu_w = 1.01-1.30$, $Re = 10^4 - 10^5$, $Pr = 3.3-34$. The errors between all simulation data points and the proposed correlation are smaller than ±5%, and the errors between 80% experiment points and the correlation are smaller than ±5%.

The new heat transfer correlation and the beneficial results can offer helps to the industrial applications of liquid salts as heat transfer mediums in energy technologies.

Acknowledgements

The study is supported by the National Natural Science Foundation of China (No.51806165) and the Key Project of National Natural Science Foundation of China (No.51436007).

The authors also thank the Science and Technology Planning Project of Xi'an (201809160CX1JC2-02)

Appendix A

Table A1. Thermophysical properties of the liquid salts and synthetic oil[35, 59, 60].

Salt	Tem. Range/K	Piecewise functions of the properties	Fusion point/K
FLiNaK	773-1170	ρ=2579.3-0.624 T, kgm^{-3}	727
	773-1080	c_p=1880, J(kgK)$^{-1}$	
	790-1080	k=0.36+5.6E-4T, W(mK)$^{-1}$	
	773-1163	μ=10$^{(-4.6044+1944/T)}$, Pas	
NaF-NaBF$_4$	673-864	ρ=2446.3-0.711T, kgm^{-3}	658
	673-1000	c_p=1506, J(kgK)$^{-1}$	
	682-1000	k=0.66-2.37E-4T, W(mK)$^{-1}$	
	682-810	μ=8.77E-5·e$^{(2240/T)}$, Pas	
Solar Salt	573-873	ρ=2263.628-0.636T, kgm^{-3}	495
	573-873	c_p=1396.044+0.172T, J(kgK)$^{-1}$	
	573-873	k=0.3911+1.9E-4T, W(mK)$^{-1}$	
	573-873	μ=0.0755-2.7761E-4T+3.4889E-7T^2-1.474E-10T^3, Pas	
Hitec	450-800	ρ=2280.22-0.733T, kgm^{-3}	415
	450-800	c_p=1560, J(kgK)$^{-1}$	
	450-536	k=2.2627-0.01176T+2.551E-5T^2-1.863E-8T^3, W(mK)$^{-1}$	
	536-800	k=0.7663-6.47E-4T, W(mK)$^{-1}$	
	450-500	μ=0.93845-5.4754E-3T, Pas	
	500-800	μ=0.23816-1.2768E-3T+2.6275E-6T^2-2.4331E-9T^3+8.507E-13T^4, Pas	
YD-325 oil	300-573	ρ=1199.13-0.6311T, kgm^{-3}	–
	300-573	c_p=776+3.4T, J(kgK)$^{-1}$	
	300-573	k=0.1416-6.68E-5T, W(mK)$^{-1}$	
	323-423	μ=0.33065-2.283E-3T+5.2746E-6T^2-4.066E-9T^3, Pas	
	423-523	μ=0.05989-3.452E-4T+6.735E-7T^2-4.413E-10T^3, Pas	

Nomenclature

A_c	inlet or outlet area, m^2
A	heat transfer area, m^2
c_1, c_2, c_3, c_μ	constants in numerical model
c_p	specific heat capacity at constant pressure, $J \cdot kg^{-1} \cdot K^{-1}$
D	inside diameter of round tube, mm
f	friction factor of flow
g	gravity ($m \cdot s^{-2}$)
h	convective heat transfer coefficient ($W \cdot m^{-2} \cdot K^{-1}$)
k	turbulent kinetic energy of flow ($m^2 \cdot s^{-2}$)
L	effective length of tube(m, mm)
Nu	nondimensional Nusselt number
Pr	nondimensional Prandtl number
p	pressure (Pa)
Pr_t	turbulent Prandtl number of energy
q	local heat flux obtained by salt ($W \cdot m^{-2}$)
Q	heat transfer rate (W)
Re	nondimensional Reynolds number
STHX	shell-tube heat exchanger
T_f	qualitative temperature of the salt (K)
$T_{f,i}$, $T_{f,o}$	temperatures at the inlet, outlet(K)
T_w	temperature of heat transfer surface (K)
T	temperature (K)
v_f	velocity of salt ($m \cdot s^{-1}$)
u, v, w	components of velocity ($m \cdot s^{-1}$)
X_t, Y_t, Z_t	Cartesian axes of tube system (m)
X_r, Y_r, Z_r	Cartesian axes of receiver system (m)

Greek symbols

δ_{ij}	unit tensor
ΔT	logarithmic temperature difference (K)
Δp	drop of pressure (Pa)
ε	turbulent dissipation rate of flow ($m^2 \cdot s^{-3}$)
λ	thermal conductivity of materials($W \cdot m^{-1} \cdot K^{-1}$)
μ_t	turbulent viscosity of flow ($kg \cdot m^{-1} \cdot s^{-1}$)
μ	dynamic viscosity of fluid (Pa·s)
ρ	density of materials ($kg \cdot m^{-3}$)
σ_ε	turbulent Prandtl number of ε
σ_k	turbulent Prandtl number of k

Subscripts

i, o, w, f	inlet , outlet , wall , fluid

References

[1] Tokarska KB, Gillett NP. Cumulative carbon emissions budgets consistent with 1.5° C global warming. Nature Climate Change. 2018;8:296.

[2] Li MJ, Tao WQ. Review of methodologies and polices for evaluation of energy efficiency in high energy-consuming industry. Appl Energ. 2017;187:203-15.

[3] Li MJ, Zhu HH, Guo JQ, Wang K, Tao WQ. The development technology and applications of supercritical CO2 power cycle in nuclear energy, solar energy and other energy industries. Appl Therm Eng. 2017;126:255-75.

[4] Ma Z, Yang WW, Yuan F, Jin B, He YL. Investigation on the thermal performance of a high-temperature latent heat storage system. Appl Therm Eng. 2017;122:579-92.

[5] Li MJ, He YL, Tao WQ. Modeling a hybrid methodology for evaluating and forecasting regional energy efficiency in China. Appl Energ. 2017;185:1769-77.

[6] He YL, Wang K, Qiu Y, Du BC, Liang Q, Du S. Review of the solar flux distribution in concentrated solar power: non-uniform features, challenges, and solutions. Appl Therm Eng. 2019;149:448-74.

[7] Wang K, He YL. Thermodynamic analysis and optimization of a molten salt solar power tower integrated with a recompression supercritical CO2 Brayton cycle based on integrated modeling. Energ Convers Manag. 2017;135:336-50.

[8] Li MJ, Jin B, Yan JJ, Ma Z, Li MJ. Numerical and Experimental study on the performance of a new two-layered high-temperature packed-bed thermal energy storage system with changed-diameter macro-encapsulation capsule. Appl Therm Eng. 2018;142:830-45.

[9] Ma Z, Li MJ, Yang WW, He YL. General performance evaluation charts and effectiveness correlations for the design of thermocline heat storage system. Chem Eng Sci. 2018;185:105-15.

[10] Li MJ, Jin B, Ma Z, Yuan F. Experimental and numerical study on the performance of a new high-temperature packed-bed thermal energy storage system with macroencapsulation of molten salt phase change material. Appl Energ. 2018;221:1-15.

[11] Lake JA. The fourth generation of nuclear power. Prog Nucl Energ. 2002;40:301-7.

[12] Romatoski RR, Hu LW. Fluoride salt coolant properties for nuclear reactor applications: A review. Ann Nucl Energy. 2017;109:635-47.

[13] He YL, Zheng ZJ, Du BC, Wang K, Qiu Y. Experimental investigation on turbulent heat transfer characteristics of molten salt in a shell-and-tube heat exchanger. Appl Therm Eng. 2016;108:1206-13.

[14] Qiu Y, Li MJ, Wang WQ, Du BC, Wang K. An experimental study on the heat transfer performance of a prototype molten-salt rod baffle heat exchanger for concentrated solar power. Energy. 2018;156:63-72.

[15] Silverman MD, Huntley WR, Robertson HE. Heat transfer measurements in a forced convection loop with two molten-fluoride salts LiF-BeF2-ThF2-UF4 and eutectic NaBF4-NaF. Oak Ridge: Oak Ridge National Laboratory; 1976, ORNL/TM-5335.

[16] Cooke JW, Cox BW. Forced-convection heat transfer measurements with a molten fluoride salt mixture flowing in a smooth tube. Oak Ridge: Oak Ridge National Laboratory; 1973, ORNL-TM-4079.

[17] Hoffman HW, Lones J. Fused salt heat transfer. Part II. Forced convection heat transfer in circular tubes containing NaF-KF-LiF eutectic. Oak Ridge: Oak Ridge National Laboratory; 1955, ORNL-1777.

[18] Grele MD, Gedeon L. Forced-convection heat-transfer characteristics of molten FLiNaK flowing in an inconel X system. Washington: National Advisory Committee for Aeronautics; 1954, RM E53L18.

[19] Vriesema B. Aspects of molten fluorides as heat transfer agents for power generation [PhD]. Delft, Netherlands: Delft University of Technology; 1979.

573 [20] Hoffman HW, Cohen SI. Fused salt heat transfer: Part III: Forced-convection heat transfer in circular tubes containing
574 the salt mixture NaNO2-NaNO3-KNO3. Oak Ridge: Oak Ridge National Laboratory; 1960, ORNL-2433.
575 [21] Kirst W, Nagle W, Castner J. A new heat transfer medium for high temperatures. Transactions of the American Institute
576 of Chemical Engineers. 1940;36:371-94.
577 [22] Wu YT, Chen C, Liu B, Ma CF. Investigation on forced convective heat transfer of molten salts in circular tubes. Int
578 Commun Heat Mass. 2012;39:1550-5.
579 [23] Du BC, He YL, Qiu Y, Liang Q, Zhou YP. Investigation on heat transfer characteristics of molten salt in a shell-and-
580 tube heat exchanger. Int Commun Heat Mass. 2018;96:61-8.
581 [24] Qian J, Kong Q, Zhang H, Huang W, Li W. Performance of a gas cooled molten salt heat exchanger. Appl Therm Eng.
582 2016;108:1429-35.
583 [25] Chen Y, Zhu H, Tian J, Fu Y, Tang Z, Wang N. Convective heat transfer characteristics in the laminar and transition
584 region of molten salt in concentric tube. Appl Therm Eng. 2017;117:682-8.
585 [26] Chen YS, Wang Y, Zhang JH, Yuan XF, Tian J, Tang ZF, et al. Convective heat transfer characteristics in the turbulent
586 region of molten salt in concentric tube. Appl Therm Eng. 2016;98:213-9.
587 [27] Wu YT, Liu B, Ma CF, Guo H. Convective heat transfer in the laminar–turbulent transition region with molten salt in
588 a circular tube. Exp Therm Fluid Sci. 2009;33:1128-32.
589 [28] Liu B, Wu YT, Ma CF, Ye M, Guo H. Turbulent convective heat transfer with molten salt in a circular pipe. Int Commun
590 Heat Mass. 2009;36:912-6.
591 [29] Sieder EN, Tate GE. Heat transfer and pressure drop of liquids in tubes. Industrial & Engineering Chemistry.
592 1936;28:1429-35.
593 [30] Gnielinski V. New equations for heat and mass transfer in turbulent pipe and channel flow. International Chemical
594 Engineering. 1976;16:359-68.
595 [31] Hausen H. Neue Gleichungen fur die Warmeubertragung bei freier oder erzwungener Stromung(New equations for
596 heat transfer in free or forced flow). Allgemeine Wärmetechnik. 1959;9:75-9.
597 [32] Bergman TL, Incropera FP. Introduction to heat transfer. Hoboken: John Wiley & Sons; 2011.
598 [33] Tao WQ. Mechanism, simulation technologies and evaluation of heat transfer enhancements for gas flow. First
599 academic conference of Aero Engine Corporation of China and Xi'an Jiaotong University, Xi'an, Sep. 24, 2017.
600 [34] Gill DD, Kolb WJ, Briggs RJ. An evaluation of pressure and flow measurement in the molten salt test loop (MSTL)
601 system. Albuquerque: Sandia National Laboratories; 2013, SAND2013-5366.
602 [35] Ferng YM, Lin KY, Chi CW. CFD investigating thermal-hydraulic characteristics of FLiNaK salt as a heat exchange
603 fluid. Appl Therm Eng. 2012;37:235-40.
604 [36] Du BC, He YL, Wang K, Zhu HH. Convective heat transfer of molten salt in the shell-and-tube heat exchanger with
605 segmental baffles. Int J Heat Mass Tran. 2017;113:456-65.
606 [37] Qiu Y, He YL, Li PW, Du BC. A comprehensive model for analysis of real-time optical performance of a solar power
607 tower with a multi-tube cavity receiver. Appl Energ. 2017;185:589-603.
608 [38] Sun F, Guo M, Wang Z, Liang W, Xu Z, Yang Y, et al. Study on the heliostat tracking correction strategies based on an
609 error-correction model. Sol Energ. 2015;111:252-63.
610 [39] Du BC, He YL, Zheng ZJ, Cheng ZD. Analysis of thermal stress and fatigue fracture for the solar tower molten salt
611 receiver. Appl Therm Eng. 2016;99:741-50.
612 [40] He YL, Xiao J, Cheng ZD, Tao YB. A MCRT and FVM coupled simulation method for energy conversion process in
613 parabolic trough solar collector. Renew Energ. 2011;36:976-85.
614 [41] Cheng ZD, He YL, Xiao J, Tao YB, Xu RJ. Three-dimensional numerical study of heat transfer characteristics in the

615 receiver tube of parabolic trough solar collector. Int Commun Heat Mass. 2010;37:782-7.
616 [42] Wang K, He YL, Cheng ZD. A design method and numerical study for a new type parabolic trough solar collector with
617 uniform solar flux distribution. SCI CHINA SER E. 2014;57:531-40.
618 [43] Qiu Y, Li MJ, He YL, Tao WQ. Thermal performance analysis of a parabolic trough solar collector using supercritical
619 CO2 as heat transfer fluid under non-uniform solar flux. Appl Therm Eng. 2017;115:1255-65.
620 [44] Zheng ZJ, He Y, He YL, Wang K. Numerical optimization of catalyst configurations in a solar parabolic trough receiver-
621 reactor with non-uniform heat flux. Sol Energ. 2015;122:113-25.
622 [45] Wang FQ, Tang ZX, Gong XT, Tan JY, Han HZ, Li BX. Heat transfer performance enhancement and thermal strain
623 restrain of tube receiver for parabolic trough solar collector by using asymmetric outward convex corrugated tube.
624 Energy. 2016;114:275-92.
625 [46] Qiu Y, He YL, Cheng ZD, Wang K. Study on optical and thermal performance of a linear Fresnel solar reflector using
626 molten salt as HTF with MCRT and FVM methods. Appl Energ. 2015;146:162-73.
627 [47] Qiu Y, He YL, Wu M, Zheng ZJ. A comprehensive model for optical and thermal characterization of a linear Fresnel
628 solar reflector with a trapezoidal cavity receiver. Renew Energ. 2016;97:129-44.
629 [48] Zhou YP, He YL, Qiu Y, Ren Q, Xie T. Multi-scale investigation on the absorbed irradiance distribution of the
630 nanostructured front surface of the concentrated PV-TE device by a MC-FDTD coupled method. Appl Energ.
631 2017;207:18-26.
632 [49] Qiu Y, Li MJ, Wang K, Liu ZB, Xue XD. Aiming strategy optimization for uniform flux distribution in the receiver of
633 a linear Fresnel solar reflector using a multi-objective genetic algorithm. Appl Energ. 2017;205:1394-407.
634 [50] Cui FQ, He YL, Cheng ZD, Li YS. Study on combined heat loss of a dish receiver with quartz glass cover. Appl Energ.
635 2013;112:690-6.
636 [51] Wang F, Guan Z, Tan J, Ma L, Yan Z, Tan H. Transient thermal performance response characteristics of porous-medium
637 receiver heated by multi-dish concentrator. Int Commun Heat Mass. 2016;75:36-41.
638 [52] Du S, Li MJ, Ren Q, Liang Q, He YL. Pore-scale numerical simulation of fully coupled heat transfer process in porous
639 volumetric solar receiver. Energy. 2017;140:1267-75.
640 [53] He YL, Cui FQ, Cheng ZD, Li ZY, Tao WQ. Numerical simulation of solar radiation transmission process for the solar
641 tower power plant: From the heliostat field to the pressurized volumetric receiver. Appl Therm Eng.2013;61:583-95.
642 [54] Wang W Q, Qiu Y, Li M J, et al. Optical efficiency improvement of solar power tower by employing and
643 optimizing novel fin-like receivers[J]. Energy Conversion and Management, 2019, 184: 219-234.
644 [55] He YL, Cheng ZD, Cui FQ, Li ZY, Li D. Numerical investigations on a pressurized volumetric receiver: Solar
645 concentrating and collecting modelling. Renew Energ. 2012;44:368-79.
646 [56] Wang K, He YL, Li P, Li MJ, Tao WQ. Multi-objective optimization of the solar absorptivity distribution inside a cavity
647 solar receiver for solar power towers. Sol Energ. 2017;158:247-58.
648 [57] Skocypec R, Romero V. Thermal modeling of solar central receiver cavities. J Sol Energ. 1989;111:117-23.
649 [58] Yu Q, Wang Z, Xu E. Simulation and analysis of the central cavity receiver's performance of solar thermal power tower
650 plant. Sol Energ. 2012;86:164-74.
651 [59] Serrano-López R, Fradera J, Cuesta-López S. Molten salts database for energy applications. Chemical Engineering and
652 Processing: Process Intensification. 2013;73:87-102.
653 [60] Beneš O, Konings RJM. Thermodynamic properties and phase diagrams of fluoride salts for nuclear applications. J
654 Fluorine Chem. 2009;130:22-9.
655 [61] Li MJ, Qiu Y, Li MJ. Cyclic thermal performance analysis of a traditional Single-Layered and of a novel Multi-Layered
656 Packed-Bed molten salt Thermocline Tank. Renew Energ. 2018;118:565-78.

[62] Cheng ZD, He YL, Cui FQ, Xu RJ, Tao YB. Numerical simulation of a parabolic trough solar collector with nonuniform solar flux conditions by coupling FVM and MCRT method. Sol Energ. 2012;86:1770-84.
[63] Chang C, Sciacovelli A, Wu Z, Li X, Li Y, Zhao M, et al. Enhanced heat transfer in a parabolic trough solar receiver by inserting rods and using molten salt as heat transfer fluid. Appl Energ. 2018;220:337-50.
[64] Tao WQ. Numerical Heat Transfer. 2nd ed. Xi'an: Xi'an Jiaotong University Press; 2001.
[65] ANSYS FLUENT 18.0 Theory Guide. ANSYS Inc. 2017.
[66] Versteeg HK, Malalasekera W. An introduction to computational fluid dynamics: the finite volume method. 2 ed ed. London: Pearson Education; 2007.
[67] Fernandez-Seara J, Uhía FJ, Sieres J, Campo A. A general review of the Wilson plot method and its modifications to determine convection coefficients in heat exchange devices. Appl Therm Eng. 2007;27:2745-57.
[68] Coleman HW, Steele WG. Experimentation, validation, and uncertainty analysis for engineers: John Wiley & Sons; 2009.
[69] Yang SM, Tao WQ. Heat transfer. 4th ed. Beijing, China: Higher Education Press; 2006.